



Creation and investigation of electronic defects on methylammonium lead iodide ($\text{CH}_3\text{NH}_3\text{PbI}_3$) films depending on atmospheric conditions

YILMAZ Gokhan^{1,a}

¹ Engineering and Architecture Faculty, Department of Energy Systems Engineering, Burdur Mehmet Akif Ersoy University, Burdur, Turkey

Received 15 March 2021 / Accepted 29 April 2021
© The Author(s) 2021

Abstract. Methylammonium lead iodide (MAPbI_3) ($\text{CH}_3\text{NH}_3\text{PbI}_3$) is popular material for edge technology application, but it still includes many uncertainties. Particularly, molecular and electronic degradation (electronic defect distribution) and mobility–lifetime product still hold many mysteries. Stemming from the atmospheric or light-induced degradation, mobility–lifetime product changes are still unknown and haven't been studied up to now. In this study, mobility–lifetime product change was investigated depending on degradation source such as atmospheric and light soaked. MAPbI_3 films were deposited by thermal chemical vapor deposition (thermal CVD). Structural analysis was done by X-ray diffraction (XRD), respectively. Deposited MAPbI_3 films were exposed to laboratory ambient, vacuum atmosphere, deionized water vapor (DIWV) atmosphere and UV light soaking at constant temperature (300K) to define changes on mobility–lifetime product.

1 Introduction

Methylammonium lead iodide (MAPbI_3) ($\text{CH}_3\text{NH}_3\text{PbI}_3$) has great electronic properties because of its long diffusion length (LD), carrier lifetime (μ) and charge carrier mobility (τ) [1–11]. These special electronic properties give opportunity to use MAPbI_3 in edge technology such as light-emitting diodes (LEDs) [12, 13], thin-film transistors (TFTs) [14], optically pumped lasers [15], photodetectors [16, 17], resistive switching random access memory (ReRAM) [18], solar water splitting [19] and photovoltaic devices [20]. However, it is known that MAPbI_3 materials have degradation problem because of stress factors such as UV light, oxygen and water vapor. Stress factors can change electronic defect states in material band gap. Electronic defect state changes can also affect the mobility–lifetime product ($\mu\tau$) of the material.

In the literature, mobility measurements generally are done by Hall effect measurements and/or TOF (time-of-flight photoconductivity) and FET (field effect transistor) technique. These techniques are known to measure transient states. However, to determine the changes in the electronic defect states due to the stress factors, the results should be obtained in the steady-state condition. Only in this way, electronic defect state changes can be comparable. In such a situation, it is easier to calculate mobility–lifetime product than mobil-

ity determination. For this reason, it is accepted as an appropriate method to obtain the mobility–lifetime product value expression from steady-state photoconductivity expressions.

In this study, MAPbI_3 films were deposited by thermal chemical vapor deposition (thermal CVD) method on microscope glass. The structure of films was examined by X-ray diffraction (XRD). To create electronic defect changes, single stress factors (vacuum atmosphere, high-purity oxygen, deionized water vapor (DIW vapor) and UV light soaking) have been applied to MAPbI_3 films. For each steady-state condition, flux-dependent photoconductivity measurements were done. Mobility–lifetime products depending on the generation rate have been calculated. The effects of stress-induced degradation on mobility–lifetime products were determined and compared.

2 Material and method

2.1 Material

MAPbI_3 films were deposited by two different temperature zones (hot zone and low zone) of thermal CVD system. Lead iodide (PbI_2) (Sigma-Aldrich %99) (6.0×10^{-4} kg) and methylammonium iodide (MAI) (Sigma-Aldrich %98) (2.5×10^{-5} kg) were used as a source material. PbI_2 was put in hot zone, and MAI

^a e-mail: gyilmaz@mehmetakif.edu.tr (corresponding author)

Table 1 MAPbI₃ films deposition temperature detail

MAPbI ₃ Code	PbI ₂ temperature	MAI temperature
20-CP-3	673 K	473 K
20-CP-7	633 K	473 K

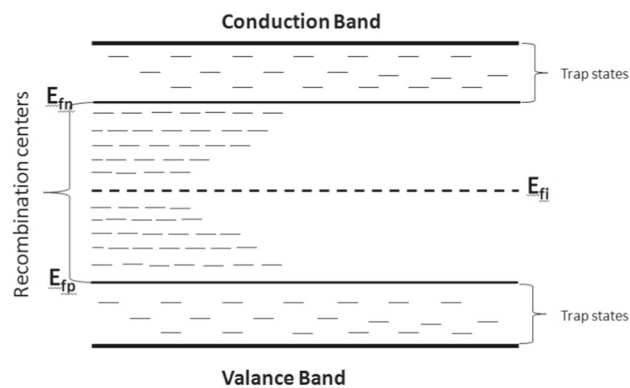
was put in low zone. MAPbI₃ films deposition temperature detail is given in Table 1.

Before the heat treatment, tube was flushed with nitrogen (N₂) to remove unintentional molecules in the system and then system was placed in vacuum (10⁻³ mbar) for 30 minutes with the mechanical pump. Afterward, the temperatures of the tube furnace were increased with proportional–integrative–derivative (PID) control from room temperature to evaporation temperatures at 10 K per minute. When the system reached evaporation temperatures, evaporated sources were carried with N₂ (200 sccm) and were deposited on glass substrate. The system was kept at evaporation temperatures for 30 minutes for deposition. After 30 minutes, system was left to cool to room temperature by itself. Coplanar metal (Ag) contact geometry was applied on MAPbI₃ films' surface with a mask by thermal evaporation. The thickness of metal contacts was 5.0 × 10⁻⁷ m, the length of contacts was 5.0 × 10⁻³ m, and gap of contacts was 5.0 × 10⁻⁴ m. MAPbI₃ films structural characterization was done by XRD. MAPbI₃ films were electrically characterized by flux-dependent photoconductivity. Three different stress factors were applied to MAPbI₃ films such as UV light soaking, high-purity oxygen gases and deionized water vapor. Each stress factor was applied at 300 K at 30 minutes. After each stress factor, annealing procedure was applied to MAPbI₃ films in vacuum. Annealing was applied between 300 K to 400 K with PID at 2 K ramp. When MAPbI₃ films reached 400 K, samples were kept for 30 minutes at this temperature for annealing.

2.2 Method

Electrical transport can occur either ionic or electronic in perovskite materials [21, 22]. When measurement temperature is close to room temperature (295 K), electronic transport gets dominant. Another critical parameter is the measurement's time range. When the measurement time is in the seconds' range, electronic transport gets dominant again [22]. Since in this study measurements have been applied at 300 K and measurements take seconds range, electronic transport was mainly taken for conductivity calculation.

Absorption of the photon, which has greater energy than the bandgap of semiconductor material, generates additional electron–hole pairs. These generated electron and holes increase the carrier concentration in conduction and valance band, respectively. When photon flux increases, quasi-Fermi level position is also changed. These quasi-Fermi level position changes also affect charge carrier concentration, traps and recombination center's concentration. In literature, Simmons

**Fig. 1** Recombination centers and trap state visualization in semiconductor materials

and Taylor's study defines these parameters changed in semiconductor materials [23]. These parameter changes are tried to be visualized in Fig. 1. As seen in Fig. 1, trap levels for electrons are between energy levels of quasi-Fermi level (Efn) and conduction band. In the same figure, trap levels for holes are between energy levels of quasi-Fermi level (Efp) and valance band. As the intensity of the light increases, the quasi-Fermi levels approach the band tails. Thus, the concentration of recombination centers also increases. When the free charge carriers are caught by these centers, the recombination process is completed and both carriers disappear. Consequently, the lifetime of free electrons and holes decreases.

Although it is perceived qualitatively that there are many electronic defects localized in the forbidden energy range in perovskite film materials, it is not possible to quantify the energy distributions, properties and densities of each. Limited methods are tried to obtain information about the existence of electronic defects and new electronic defects created by the effect of metastability. Flux-dependent steady-state photoconductivity measurements can detect changes that may occur in the concentration of existing electronic defects.

In photoconductivity measurements, the increase in flux causes an increase in the generation rate (G) of electrons–holes. As a result, the quasi-Fermi levels (Efn and Efp) move toward the conduction and valance band edges, respectively. With the movement of the quasi-Fermi levels toward the band edges, some of the trap turns into recombination centers. In Fig. 2, traps change (turning into recombination center) is tried to be visualized. In Fig. 2, when the flux is increased from G1 to G3 at constant temperature T1, the Efn and Efp quasi-Fermi levels are again expanded toward the band edges and the localized electronic defects within the bandgap energy range are detected by photoconductivity measurements.

In the steady state, the electron-hole generation rate (G), which is controlled externally, and the (U) recombination rates controlled by the inside of the material are equal. In the Simmons–Taylor equation, at steady-state condition, generation rate (G) is equal to recom-

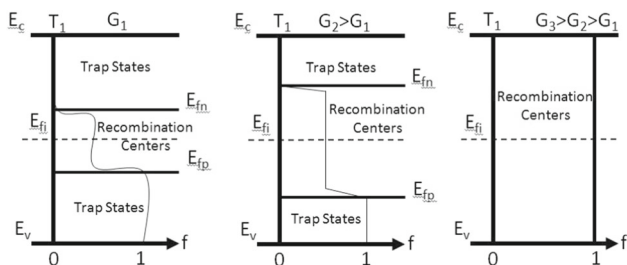


Fig. 2 Recombination centers and trap state change depending on generation rate at constant temperature in semiconductor materials

bination rate (U); at that situation, free electron concentration n (G) and free hole concentration p (G) can be determined from the experimentally measured photoconductivity and expressed in Eq. 1.

$$\sigma(ph) = q\mu_n n(G) + q\mu_p p(G) \tag{1}$$

In this equation, it is determined by $n(G)=\tau_n G$ and $p(G)=\tau_p G$. If these expressions are added to Eq. 1, the photoconductivity equation becomes

$$\sigma(ph) = q\mu_n \tau_n G + q\mu_p \tau_p G \tag{2}$$

where G is the function of electron-hole recombination rate. Also, it can be assumed that $\mu_n \tau_n \gg \mu_p \tau_p$ for free electrons and holes since the distributions of electronic defects present in the bandgap energy range of perovskite materials are asymmetrical and besides electronic defects close to the valence band edge have a higher concentration. For this reason, photoconductivity consists of electrons that dominated one type of charge carriers.

$$\sigma(ph) \approx q\mu_n \tau_n G \tag{3}$$

If the left side of the equation is the photoconductivity findings obtained experimentally depending on the flux, the mobility–lifetime of free electrons, $\mu_n \tau_n$, is obtained from here:

$$\mu_n \tau_n = \sigma(ph)/qG \tag{4}$$

Electron–hole generation rate (G) is determined entirely by the experimental conditions and the properties of the material under single wavelength. Generation rate can be calculated from Eq. 5.

$$G = (F(\lambda)[1 - R(\lambda)][1 - exp(-\alpha t)])/t \tag{5}$$

In Eq. 5, t is thickness of material, α is absorption coefficient at constant wavelength, R is the reflection of material at constant wavelength, and F is the flux of constant wavelength. Incident light flux can be calculated as in Eq. 6.

$$F(\lambda) = I_{ph}(\lambda)/(A.QE(\lambda).q) \tag{6}$$

In Eq. 6, I_{ph} is short circuit current of photodetector at incident light wavelength, A is area of detector, QE is quantum efficiency of detector at incident light wavelength, and q is the elemental charge.

In this study, 120V 250W Osram ENH halogen bulb was used as a light source. In order to increase flux value, 10cm focal distance lens and flux calibration Newport metallic neutral density filters (1.0 OD, 2.0 OD, 0.5 OD, 0.3 OD) combination was used. For specific wavelength Newport 630nm bandpass filter was used. Hamamatsu S2386-44K photodetector was used as a calibration photodetector.

3 Results and discussion

3.1 Structural characterization

XRD measurements were done by Bruker AXS D8 Advance measuring system, and Cu tube was used for X-ray source. Measurements were carried out in the 2 theta range from 0 to 70 degrees. The X-ray patterns obtained were refined with the FullProf program and the profile matching method. In Fig. 3 two crystalline phases are observed in 20-CP-3. Observed and calculated XRD pattern was matching each other. Chi-square value was observed 3.69 from FullProf program. These phases are in the space group Pnma orthorhombic and I4/mcm tetragonal, belonging to the MAPbI3 structure observed in the literature [3, 4, 7, 24]. The calculated RF factors of the two patterns are 3.17 and 3.82, respectively. The two crystal structures are found in 54% and 46% of the main pattern. The lattice parameters obtained for the orthorhombic phase were found as: $a = 8.927$, $b = 12.650$ and $c = 8.409$ Angstroms. The lattice parameters for the tetragonal phase are $a = b = 9.443$ and $c = 12.188$ Angstroms. The crystal structure has a dominant preferred orientation in the direction of the plane (521) (52 degrees peak).

The 20-CP-7 sample was crystallized in a single phase according to the other sample and has a tetragonal structure of I4 / mcm. The value of χ^2 was found to be 1.13. The lattice parameters obtained for the tetragonal phase were $a = b = 9.445$ and $c = 12.116$ Angstroms. This tetragonal structure has a strong orientation only in the (110) plane.

3.2 Electrical characterization

In Fig. 4 laboratory aged state and annealed-1 state mobility–lifetime results are given for samples 20-CP-3 and 20-CP-7. As seen in 20-CP-3, laboratory aged state values and annealed-1 state values were close to each other. On the other hand, a significant decrease in $\mu\tau$ values on low generation rate region (10^{19}) was observed after first heat treatment.

In Fig. 4, in 20-CP-7, there was a sharp difference between the laboratory aged state and the annealed-1 state. After the heat treatment, almost one order of

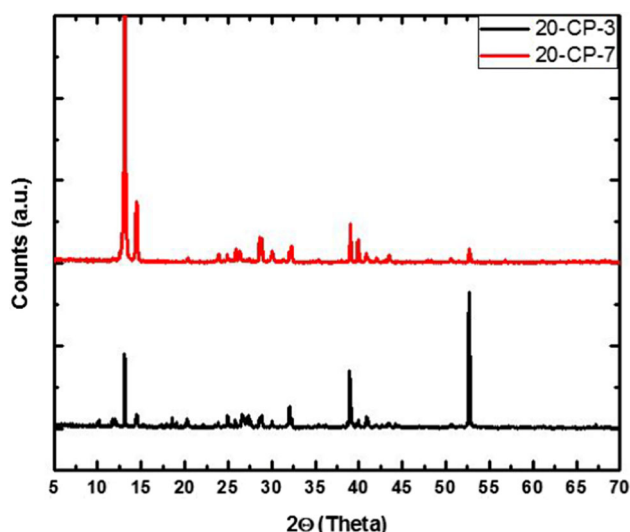


Fig. 3 20-CP-3 and 20-CP-7 MAPbI₃ films XRD pattern

magnitude increase was observed on $\mu\tau$ values. The only reason for the change in the $\mu\tau$ values, between laboratory aged state and annealed-1 state, is the electronic defects created by the molecules attached to the materials in the laboratory atmosphere for both materials.

Annealed-1 state is the most important state in aging studies. Annealed-1 state is generally defined as the as-grown state of materials. For this reason, after each applied stress factor, a comparison was made with annealed-1 state. After the first annealing, the materials were exposed to UV light for 30 minutes in a vacuum atmosphere. The changes in $\mu\tau$ values due to UV light are presented in Fig. 5 for both material. As can be seen in Fig. 5, after UV application, $\mu\tau$ values significantly decrease for both material compared to annealed-1 state. Only in the high generation rate region (10^{21}), sample 20-CP-7, the $\mu\tau$ values were exceeded over annealed-1 state after UV light application. This indicates that $\mu\tau$ values were determined from trap states in the low generation rate (10^{19}) region for 20-CP-7. However, in the high generation rate (10^{21}) region, there was a decrease in the recombination centers according to the annealed-1 state due to UV light and this reduction determined the $\mu\tau$ values change. After the second annealing, a net $\mu\tau$ value increase was determined in the 20-CP-3 in Fig. 5. This increase exceeded the annealed-1 state values in the high generation rate (10^{21}) region. This shows that a certain part of the recombination centers was reduced by second annealing. In Fig. 5, in 20-CP-7, it was observed that after UV application $\mu\tau$ values decreased but with the second annealing $\mu\tau$ values increased in the low generation rate (10^{19}) region. However, it was seen that $\mu\tau$ values decrease in the high generation rate (10^{21}) region after the second annealing. This situation can be interpreted as the increase in recombination centers with the second heat treatment in the high generation rate (10^{21}) region.

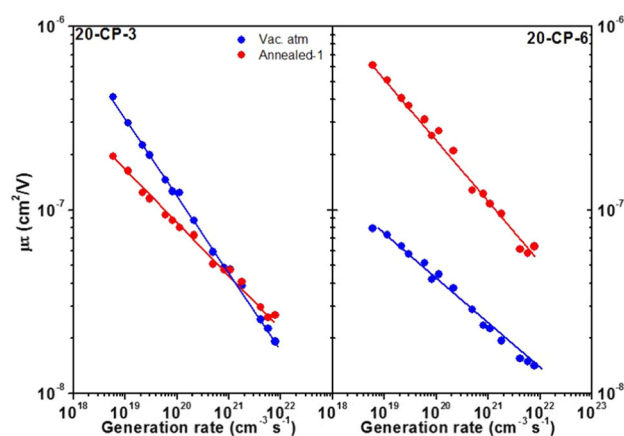


Fig. 4 Laboratory aged state vacuum atmosphere and annealed-1 state vacuum atmosphere mobility–lifetime products of 20-CP-3 and 20-CP-7

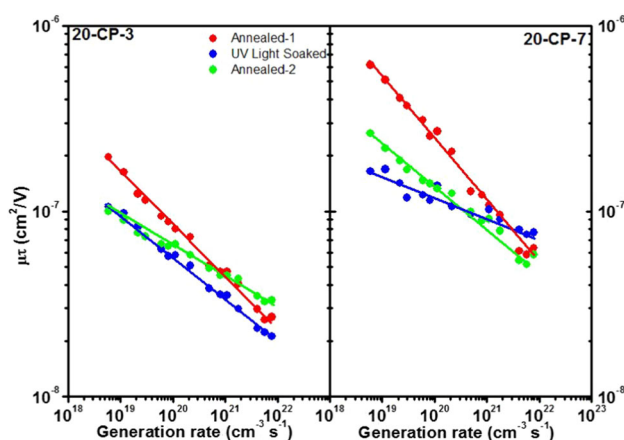


Fig. 5 UV aged state vacuum atmosphere, annealed-1 state vacuum atmosphere and annealed-2 state vacuum atmosphere mobility–lifetime products of 20-CP-3 and 20-CP-7

After the second annealed state, both materials were exposed to high purity (%99,99) oxygen gas without breaking the vacuum atmosphere. The materials waited in the oxygen gas atmosphere for 30 minutes under positive pressure, and then the system was taken into the vacuum environment and $\mu\tau$ measurements were carried out. Oxygen aged state $\mu\tau$ values are presented in Fig. 6 for sample 20CP-3 and 20-CP-7.

For 20-CP-3, due to the oxygen aging, obtained $\mu\tau$ values have approached to the UV aged state values. After the third annealing, there has been almost no change in $\mu\tau$ values in the low generation rate (10^{19}) region. However, it has been determined that there is a decrease in $\mu\tau$ values in the high generation rate (10^{22}) region after third annealing. In Fig. 6, sample 20-CP-7, after oxygen gas aging, $\mu\tau$ values increased to the values obtained in first annealed state. However, this oxygen-induced $\mu\tau$ value increase has eliminated with the third annealing. Even the $\mu\tau$ values obtained in

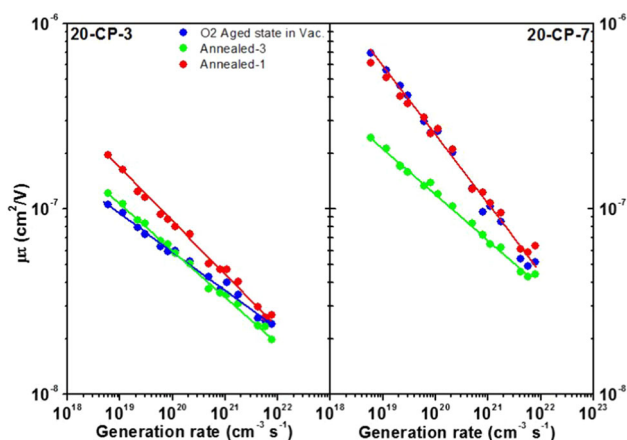


Fig. 6 Oxygen aged state vacuum atmosphere, annealed-1 state vacuum atmosphere and annealed-3 state vacuum atmosphere mobility–lifetime products of 20-CP-3 and 20-CP-7

the third annealing have matched with the $\mu\tau$ values obtained from the second annealing.

The most significant $\mu\tau$ values change in the 20-CP-3 was observed after DIW vapor application. As can be seen in Fig. 7, after DIW vapor application, there was a one-order of magnitude decrease in $\mu\tau$ values at the low generation rate (10^{19}) region, while there was a two times decrease in $\mu\tau$ values at the high generation rate (10^{22}) region. After the fourth annealing, there was a significant increase in $\mu\tau$ values especially in the low generation rate (10^{19}) region, and the effect caused by the DIW vapor was partially eliminated. This indicates that the recombination center concentration increased in 20-CP-3 due to the DIW vapor. However, it was observed that $\mu\tau$ values increased with the fourth annealing. Therefore, a certain part of the recombination center concentration was decreased with the fourth annealing. In Fig. 7, 20-CP-7 after DIW vapor application the $\mu\tau$ values of the sample increased and approached the values obtained in the case of annealed-1 state. However, after the fourth annealing, $\mu\tau$ values decreased in the low and middle generation rate region (10^{19} – 10^{20}) and returned to the values in annealing-2 and annealing-3. This situation shows that in 20-CP-7, there was a decrease in the recombination center concentration due to the DIW vapor, but some of these centers come back with fourth annealing.

4 Conclusions

The nature and types of electronic defects (recombination centers) distributions of perovskite materials with a heterogeneous structure remain uncertain. Besides, there hasn't been found a study in the literature on the relationship between electronic defect distributions of perovskite materials related with stress factor aging. This study will fill the gap in the literature by establish-

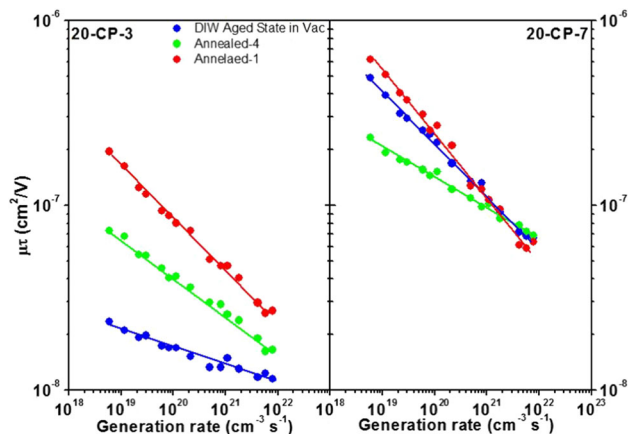


Fig. 7 DIW vapor aged state vacuum atmosphere, annealed-1 state vacuum atmosphere and annealed-4 state vacuum atmosphere mobility–lifetime products of 20-CP-3 and 20-CP-7

ing a link between the stress factors and the change in the electronic defect states of the perovskite material.

As a conclusion, it was observed that there were significant changes in $\mu\tau$ values depending on the stress factors. In regions where the generation rate is low, both recombination centers (electronic defects) and trap states constitute the change in $\mu\tau$. When the generation rate increases, trap states transform to electronic defects in the band gap. This transformation is the main source of determination of $\mu\tau$ in high generation rates. However, with annealing, there are changes in electronic defect conditions and types. This change was determined by measuring different $\mu\tau$ values even if the same annealing was applied after the stress factor. This shows that the concentration and types of electronic defect states change due to stress factors in the band gap.

Acknowledgements This study was funded by “The Scientific And Technological Research Council Of Turkey (TUBITAK)” with Project number 119F033. Some pieces of equipment used in this research are founded by project 2017K12 number as 41003-12 named as “Burdur Mehmet Akif Ersoy University, Regional Development Focus Mission Differentiation and Specialization Programme: Increasing Sectoral Competition Power in Burdur Province/Energy Division” Depending upon Presidency of Turkish Republic, Chairmanship of Presidential Strategy and Budget. The author would like to thank to Forschungszentrum Jülich/Germany and Dr. Friedhelm FINGER for donation of laboratory equipments. The author also would like to thank Prof.Dr. Fatih Mehmet EMEN and Assist. Prof. Dr. Murat KALELİ for endless fruitful academic discussions. The names Dr. Atakan TEKGÜL, B.Sc. Ayşegül ÇOŞGUN, and Dr.Serkan KOÇ should be remarked and thanked for XRD analysis, conductivity measurements and proofreading. This work benefited from networking activities carried out within the EU funded COST Action CA17126 “Toward Understanding and Modelling Intense Electronic Excitation” and represents a contribution to it.

Data Availability Statement This manuscript has no associated data or the data will not be deposited. [Authors' comment: In conclusion part general behaviour trends of samples were mentioned. If we check graphs, stress factor can increase the mu-tao values however, same stress factor can decrease mu-tao values of other sample. Thus, in these stress factors author can only mention about change of defects rather than values itself. Stress factors can change electronic defects and types but for each samples electronic defects values and types can be different.]

Declarations

Conflict of interest The author declares that they have no known competing financial interests or personal relationships that could have appeared to influence the work reported in this paper.

Open Access This article is licensed under a Creative Commons Attribution 4.0 International License, which permits use, sharing, adaptation, distribution and reproduction in any medium or format, as long as you give appropriate credit to the original author(s) and the source, provide a link to the Creative Commons licence, and indicate if changes were made. The images or other third party material in this article are included in the article's Creative Commons licence, unless indicated otherwise in a credit line to the material. If material is not included in the article's Creative Commons licence and your intended use is not permitted by statutory regulation or exceeds the permitted use, you will need to obtain permission directly from the copyright holder. To view a copy of this licence, visit <http://creativecommons.org/licenses/by/4.0/>.

References

- D.D. Li, W.L. Chen, X.L. Xu, F. Jiang, L. Wang, Y.Y. Xie, X.J. Zhang, X.K. Guo, Q.D. You, H.P. Sun, *Eur. J. Med. Chem.* **118**, 1–8 (2016)
- E.M. Hutter, G.E. Eperon, S.D. Stranks, T.J. Savenije, *J. Phys. Chem. Lett.* **6**, 3082–3090 (2015)
- Y. Deng, E. Peng, Y. Shao, Z. Xiao, Q. Dong, J. Huang, *Energy Environ. Sci.* **8**, 1544–1550 (2015)
- H. Oga, A. Saeki, Y. Ogomi, S. Hayase, S. Seki, *J. Am. Chem. Soc.* **136**, 13818–13825 (2014)
- Z. Lian, Q. Yan, T. Gao, J. Ding, Q. Lv, C. Ning, Q. Li, J.L. Sun, *J. Am. Chem. Soc.* **138**, 9409–9412 (2016)
- Y. Mei, C. Zhang, Z.V. Vardeny, O.D. Jurchescu, *J. MRS Commun.* **5**, 297–301 (2015)
- X.Y. Chin, D. Cortecchia, J. Yin, A. Bruno, C. Soci, *Nat. Commun.* **6**, 1–9 (2015)
- Z. Guo, J.S. Manser, Y. Wan, P.V. Kamat, L. Huang, *Nat. Commun.* **6**, 4–11 (2015)
- F. Li, C. Ma, H. Wang, W. Hu, W. Yu, A.D. Sheikh, T. Wu, *Nat. Commun.* **6**, 1–8 (2015)
- S.D. Stranks, G.E. Eperon, G. Grancini, C. Menelaou, M.J.P. Alcocer, T. Leijtens, L.M. Herz, A. Petrozza, H.J. Snaith, *Science* **342**, 341–344 (2013)
- C. Motta, F. El-Mellouhi, S. Sanvito, *Sci. Rep.* **5**, 1–8 (2015)
- Z.-K. Tan, R.S. Moghaddam, M.L. Lai, P. Docampo, R. Higler, F. Deschler, M. Price, A. Sadhanala, L.M. Pazos, D. Credgington, F. Hanusch, T. Bein, H.J. Snaith, R.H. Friend, *Nat. Nanotechnol.* **9**, 687–692 (2014)
- H. Cho, S.H. Jeong, M.H. Park, Y.H. Kim, C. Wolf, C.L. Lee, J.H. Heo, A. Sadhanala, N.S. Myoung, S. Yoo, S.H. Im, R.H. Friend, T.W. Lee, *Science* **350**, 1222–1225 (2015)
- Y. Wu, J. Li, J. Xu, Y. Du, L. Huang, J. Ni, H. Cai, J. Zhang, *RSC Adv.* **6**, 16243–16249 (2016)
- F. Deschler, M. Price, S. Pathak, L.E. Klintberg, D.D. Jarausch, R. Higler, S. Hüttner, T. Leijtens, S.D. Stranks, H.J. Snaith, M. Atatüre, R.T. Phillips, R.H. Friend, *J. Phys. Chem. Lett.* **5**, 1421–1426 (2014)
- T. Moehl, J.H. Im, Y.H. Lee, K. Domanski, F. Giordano, S.M. Zakeeruddin, M.I. Dar, L.P. Heiniger, M.K. Nazeeruddin, N.G. Park, M. Grätzel, *J. Phys. Chem. Lett.* **5**, 3931–3936 (2014)
- Q. Lin, A. Armin, P.L. Burn, P. Meredith, *Nat. Photonics* **9**, 687–694 (2015)
- C. Gu, J.S. Lee, *ACS Nano* **10**, 5413–5418 (2016)
- Y.S. Chen, J.S. Manser, P.V. Kamat, *J. Am. Chem. Soc.* **137**, 974–981 (2015)
- A. Kojima, K. Teshima, Y. Shirai, T. Miyasaka, *J. Am. Chem. Soc.* **131**, 6050–6051 (2009)
- Y. Lin, Y. Bai, Y. Fang, Q. Wang, Y. Deng, J. Huang, *ACS Energy Lett.* **2**, 1571–1572 (2017)
- Y.-C. Zhao, W.-K. Zhou, X. Zhou, K.-H. Liu, D.-P. Yu, Q. Zhao, *Light Sci. Appl.* **6**, 16243–1624X (2017)
- G. Taylor, J. Simmons, *J. Non-Cryst. Solids* **8–10**, 940–946 (1972)
- J.A. Christians, P.A. Miranda Herrera, P.V. Kamat, *J. Am. Chem. Soc.* **137**, 1530–1538 (2015)